Modeling and simulation of Compton scatter image formation in positron emission tomography

Kazantsev, Ivan G.; Matej, Samuel; Lewitt, Robert M.; Olsen, Ulrik L.; Poulsen, Henning F.; Yarovenko, Ivan P.; Prokhorov, Igor V.

Published in:
Journal of Inverse and Ill-Posed Problems

Link to article, DOI:
10.1515/jiip-2020-0052

Publication date:
2020

Document Version
Peer reviewed version

HHS Public Access
Author manuscript
J Inverse Ill Posed Probl. Author manuscript; available in PMC 2021 December 01.

Published in final edited form as:
J Inverse Ill Posed Probl. 2020 December ; 28(6): 923–932. doi:10.1515/jiip-2020-0052.

Modelling and Simulation of Compton Scatter Image Formation in Positron Emission Tomography

Ivan G. Kazantsev,
Institute of Computational Mathemtics and Mathematical Geophysics, 630090 Novosibirsk, Russia

Samuel Matej,
University of Pennsylvania, Department of Radiology, Philadelphia, PA 19104, USA

Robert M. Lewitt,
University of Pennsylvania, Department of Radiology, Philadelphia, PA 19104, USA

Ulrik L. Olsen,
Technical University of Denmark, Department of Physics, Fysikvej 307, 2800 Kgs. Lyngby, Denmark

Henning F. Poulsen,
Technical University of Denmark, Department of Physics, Fysikvej 307, 2800 Kgs. Lyngby, Denmark

Ivan P. Yarovenko,
Institute of Applied Mathematics, 7 Radio, 690041, Vladivostok, Russia

Igor V. Prokhorov
Institute of Applied Mathematics, 7 Radio, 690041, Vladivostok, Russia

Abstract

We present the comparative study of the analytical forward model and the statistical simulation of the Compton single scatter in the Positron Emission Tomography. The formula of the forward model has been obtained using the Single Scatter Simulation approximation under simplified assumptions and therefore we calculate scatter projections using independent Monte Carlo simulation mimicking the scatter physics. The numerical comparative study has been performed using a digital cylindrical phantom filled in with water and containing spherical sources of emission activity located at the central and several displaced positions. Good fits of the formula-based and statistically generated profiles of scatter projections are observed in the presented numerical results.

Keywords

Positron emission tomography; Compton single scatter; analytical forward model; Monte Carlo simulation; 44A12; 44A35; 45H05; 65M38; 65N21

kazantsev.ivan6@gmail.com .

1 Introduction

This paper is aimed at the comparative study of the analytical model of the Compton single scatter projection formation in Positron Emission Tomography (PET) [14] and numerical modelling the Compton image using Monte Carlo (MC) simulation [15], [30]. The model belongs to a modality what is nowadays known as Compton Scatter Tomography (CST) [11], [26], has the form of an integral transform and its derivation is based on the Single Scatter Simulation (SSS) approximation [27]. While the SSS approximation estimates a single scatter coincidence rate detected within finite detector elements for a range of energies, the analytical model provides a sample value of the scatter for a certain energy detected at a given point of the detector. That is, in the analytical model the detector system has excellent energy resolution. It is assumed that the directions of the two annihilation photons are collinear and the detectors count all incoming single scattered photons of a certain energy, or equivalently, the photons scattered once at a certain angle. For practical aspects of the scatter models in PET, we refer the reader to [2] and the literature therein.

Let us introduce the notations and briefly describe the conventional PET using non-scatters as an example of an analytical model with idealized mathematical assumptions [20]. Given an object with the activity distribution f and the attenuation map μ, and the point-wise detectors A and B (Figure 1 (a)), recorded primary data are simulated in PET as

$$P^{AB} = e^{-\int_A^B \mu(x', y', z')dl'} \int_A^B f(x, y, z)dl \tag{1.1}$$

where (x', y', z'), (x, y, z) are the points on the line AB and dl, dl' are the elements of the line AB. Equation (1.1) factorizes integrals over the activity f and the attenuation μ, thus reducing the problem to the classical computerized tomography provided that the data P^{AB} undergo the attenuation correction [3]. A physical feature of PET is basically a large amount of photon pairs (u, v), collinearly traveling in opposite directions from the annihilation point C, where a positron resulting from the isotope decay meets some of free electrons of the media μ.

In addition to the primary photons, there are photons v' with the energies $E' < E$ (E is the emitted photon energy) that undergo the Compton scatter (Figure 1 (b), (c)), and are associated with the scattering angle θ by the Compton relation:

$$E' = \frac{E}{1 + (E/511keV)(1 - \cos\theta)} . \tag{1.2}$$

Much efforts have been invested into the scatter correction of the PET data [5], [31]. In comparison with the scatter correction methods, our motivation is to create a basis for the full 3D reconstruction of activity directly from the Compton single scatter data. For this purpose, the SSS model was chosen due to its universality in covering most of the PET physics. We summarize the SSS approximation in the form of the Watson scatter formula [27]. The SSS approximation formula estimates the expected total single scatter coincidence rate in the detector pair (A, B) as an integral over the total scatter volume V

$$S_V^{AB} = \int_V dV \frac{\sigma_{AS}\sigma_{SB}}{4\pi|AS|^2|SB|^2}\frac{\mu}{\sigma_C}\frac{\partial\sigma_C}{\partial\Omega}(\epsilon_A I^A + \epsilon_B I^B), \tag{1.3}$$

where

$$I^A = e^{-(\int_A^S \mu dl + \int_S^B \mu' dl)} \int_A^S f dl,\ I^B = e^{-(\int_A^S \mu' dl + \int_S^B \mu dl)} \int_S^B f dl\,. \tag{1.4}$$

Here $\frac{\partial\sigma_C}{\partial\Omega}$ is the differential cross-section given by the Klein-Nishina formula [6], σ_{AS} and σ_{SB} are geometric cross-sections of the detectors A and B, f is the emitter activity, $\mu = \mu(E, S)$ is the linear attenuation coefficient depending on the photon energy E and the scatter point S, $\epsilon_A = \epsilon_{AS}\epsilon'_{SB}$ and $\epsilon_B = \epsilon'_{AS}\epsilon_{SB}$ are related to the detection efficiency for the detectors A and B. Primed and unprimed quantities are evaluated at the scattered and unscattered photon's energy, respectively.

Equation (1.3) is symmetric in terms of A and B so that the primary photons are recorded both at A and B. In derivation of the analytical model, a one-sided version of (1.3) was investigated, where only one detector element A is tuned to counting the primary photons. In this case, in (1.4) we can set $I^B = 0$. Using this condition, the model as a particular case of the SSS algorithm was derived [14] in the form of the integral transform as we outline in Section 2. Because of the idealized assumptions involved in the derivation of analytical scatter projector, we compare this model with Monte Carlo simulation [4], [7], [15], [30]. The MC technique can take into account every technical detail of the photon transport. The MC statistical simulation techniques are common for the verification of scatter models. Reference [31] states: "Nevertheless, the complexity and computing requirements of Monte Carlo simulation led to the development of analytical simulation tools based on simplifying approximations to improve speed of operation".

The paper is organized as follows. In Section 2 we present an analytical model of Compton single scatter obtained using the SSS algorithm as a starting point. Section 3 is devoted to the three-dimensional slice-by-slice convolution model as a partial case assuming that the attenuation map of the object is a constant term approximated to be the same for direct and scattered events. In Section 4 we outline steps of Monte Carlo simulation algorithm. Computer-based experiments with a numerical phantom are presented in Section 5 with the following discussion and conclusions Sections 6 and 7, respectively.

2 The forward model of Compton single scatter

Let us overview the derivation of the Compton analytic scatter equation for a given particular scattering angle. The following basic geometric observations [17], [21] are useful in the single scatter simulation. It is easily seen (Figure 1 (b), (c)) that all the scatter points S (at some scattering angle θ) are located on an equi-scatter isogonic surface Σ_θ of a spindle-shaped body V_θ generated by the rotated arcs $\widetilde{ASB}$ with the fixed detectors A and B. The arcs are parts of circles with the same diameter $d = |AB|/\sin\theta$ and subtended by the angle 2θ. Geometry of the spindle-shaped isogonic rotation body is desribed also in [23], [25], [28], [29]. Due to the Law of Sines for ΔASB we have

$$|AS|/\sin(\theta - \varphi) = |SB|/\sin(\varphi) = |AB|/\sin(\pi - \theta), \tag{2.1}$$

and we can write

$$|AS| = |AB|\frac{\sin(\theta - \varphi)}{\sin\theta}, |SB| = |AB|\frac{\sin\varphi}{\sin\theta}. \tag{2.2}$$

Let us for brevity denote, omitting some dependencies:

$$W_{f,\mu,\mu'}(x, y, z) \equiv \frac{1}{\sigma_C}\frac{\partial\sigma_C}{\partial\Omega}\epsilon_A\mu(x, y, z)e^{-(\int_A^S \mu dl + \int_S^B \mu' dl)}\int_A^S f dl, \tag{2.3}$$

where (x, y, z) are the Cartesian coordinates of the scatter point S. Thus, we transform equation (1.3) to a more compact form

$$S_V^{AB} = \int_V dV \frac{\sigma_{AS}\sigma_{SB}}{4\pi|AS|^2|SB|^2} W_{f,\mu,\mu'}(x, y, z). \tag{2.4}$$

The SSS approximation is sufficiently generic to deal with the scatter volume V (or, equivalently, an integration domain $D(\mu)$, or a support of the attenuation map μ) of an arbitrary shape. However, for the purposes of this research, a precise boundary of the V (and the limits in volume integral (2.4)) should be explicitly specified as well as a system of coordinates needs to be chosen.

Let us assume that the detectors A and B are small disks of radius $\delta \ll 1$, normal to the direction z, with centers at points $A = (0, 0, 0)$ and $B = (0, 0, |AB|)$, respectively (Figure 1 (c)). The detector B records the photons scattered under the scattering angles θ such that $\theta \leq T$, for some angle $T \leq \pi/2$. We find it useful to exploit the spherical coordinates (ψ, φ, r) with the origin at the point A for describing the equi-scatter surface Σ_θ and the scatter volumes V_θ and V_T:

$$\begin{aligned}
&\Sigma_\theta = \left\{(\psi, \varphi, r) \middle| \psi \in [0, 2\pi), \varphi \in [0, \theta], r = |AS|\right\},\\
&V_\theta = \left\{(\psi, \varphi, r) \middle| \psi \in [0, 2\pi), \varphi \in [0, \theta], 0 \leq r \leq |AS|\right\},\\
&V_T = \bigcup_{\theta = 0}^{T} V_\theta, |AS| = |AB|\sin(\theta - \varphi)/\sin\varphi.
\end{aligned} \tag{2.5}$$

For small values of diameter δ of detector disks A and B, the geometrical cross-sections of A and B incident to the rays AS and SB are ellipses with approximate area, respectively

$$\sigma_{AS} \approx \left(\pi\delta^2/4\right)\cos\varphi, \sigma_{SB} \approx \left(\pi\delta^2/4\right)\cos(\theta - \varphi)\,. \tag{2.6}$$

The idealized model for the total scatter (parameterized by the T and denoted as S_T^{AB}) has been developed using the SSS integral (2.4) calculated at points within the small detectors A and B, and then averaged over (A, B) disks area as follows

$$S_T^{AB} = \lim_{\delta \to 0} \frac{1}{\left(\pi\frac{\delta^2}{4}\right)^2} \int_A \int_B dAdB \int_{V_T} dV_T \frac{\sigma_{AS}\sigma_{SB}}{4\pi|AS|^2\,|SB|^2} W_{f,\mu,\mu'}(x, y, z)\,. \tag{2.7}$$

Substituting (2.6) into (2.7), we estimate the total single scatter in the form

$$S_T^{AB} = \int_{V_T} dV_T \frac{\cos\varphi\cos(\theta - \varphi)}{4\pi|AS|^2\,|SB|^2} W_{f,\mu,\mu'}(x, y, z)\,. \tag{2.8}$$

We change the rectangular variables (x, y, z) in (2.8) for other (spherical-like) curvilinear coordinates (ψ, φ, θ), where ψ, φ are the spherical coordinates and $\theta \in [0, T]$ is the scattering angle (while the distance $|AB|$ is fixed), as follows

$$\begin{Bmatrix} x = X(\psi, \varphi, \theta) = |AS|\sin\varphi\cos\psi, \\ y = Y(\psi, \varphi, \theta) = |AS|\sin\varphi\sin\psi, \\ z = Z(\psi, \varphi, \theta) = |AS|\cos\varphi\,. \end{Bmatrix} \tag{2.9}$$

For changing variables in (2.8), we calculate the elementary volume

$$dV_T = dxdydz = \left|J\right| d\psi d\varphi d\theta, \tag{2.10}$$

where J is the Jacobian matrix

$$J = \begin{bmatrix} \partial X/\partial\psi & \partial X/\partial\varphi & \partial X/\partial\theta \\ \partial Y/\partial\psi & \partial Y/\partial\varphi & \partial Y/\partial\theta \\ \partial Z/\partial\psi & \partial Z/\partial\varphi & \partial Z/\partial\theta \end{bmatrix} \tag{2.11}$$

and $|J|$ is its determinant. Due to (2.2), we have

$$|J| = \frac{AB\Big|^3 \sin^2(\varphi)\sin^2(\theta - \varphi)}{\sin^4(\theta)} = \frac{\left|AS\right|^2\left|SB\right|^2}{|AB|}, \tag{2.12}$$

and (2.8) becomes

$$S_T^{AB} = \int_0^T d\theta \int_0^\theta d\varphi \int_0^{2\pi} d\psi \frac{\cos\varphi\cos(\theta - \varphi)}{4\pi|AB|} W_{f,\mu,\mu'}(\psi, \varphi, \theta) . \tag{2.13}$$

Finally, we derive the total scatter equation under further idealized assumptions $\epsilon_A \equiv 1$ in the following integral form:

$$S_T^{AB} = \int_0^T d\theta \int_0^\theta d\varphi \frac{\cos\varphi\cos(\varphi - \theta)}{4\pi|AB|} \int_0^{2\pi} d\psi \frac{1}{\sigma_C} \frac{\partial\sigma_C}{\partial\Omega} \times \mu(\psi, \varphi, |AS|) e^{-\left(\int_A^S \mu dl + \int_S^B \mu' dl\right)} \int_0^{|AS|} f(\psi, \varphi, r) dr, \tag{2.14}$$

where the integrand in $S_T^{AB} \equiv \int_0^T \xi_\theta^{AB} d\theta,$

$$\xi_\theta^{AB} = \frac{1}{4\pi|AB|} \int_0^\theta d\varphi \cos\varphi\cos(\varphi - \theta) \int_0^{2\pi} d\psi \frac{1}{\sigma_C} \frac{\partial\sigma_C}{\partial\Omega} \times \mu(\psi, \varphi, |AS|) e^{-\left(\int_A^S \mu dl + \int_S^B \mu' dl\right)} \int_0^{|AS|} f(\psi, \varphi, r) dr \tag{2.15}$$

is a sample value of the scatter. Here θ and E' are fixed, therefore the factor $\frac{1}{\sigma_C}\frac{d\sigma_C}{d\Omega}$ in (2.15) is a scalar and for brevity can be omitted without loss of generality. A result similar to (2.15) was received in [12] using geometrical probabilities approach.

3 Slice-by-slice Convolution Blurring Model

An essential simplification can be achieved assuming $\mu = \mu' = const$. Then equation (2.15) can be written down in the cylindrical coordinates (ψ, ρ, z) after some algebra as follows

$$\xi_\theta^{AB} = \int_0^{|AB|} dz \int_0^{R_\theta(z)} d\rho \frac{\mu z(z\cos\theta + \rho\sin\theta)}{4\pi|AB|\rho\left(z^2 + \rho^2\right)^{3/2}} e^{-\mu|AB| \frac{z + \rho\tan\frac{\theta}{2}}{\sqrt{z^2 + \rho^2}}} \int_0^{2\pi} d\psi f(\psi, \rho, z), \tag{3.1}$$

where radius of the circular section of V_θ with the coordinate z is

$$R_\theta(z) = \frac{\sqrt{a^2 - (z - a)^2\sin^2\theta} - a\cos\theta}{\sin\theta}, a \equiv \frac{|AB|}{2} . \tag{3.2}$$

Multiplying equation (3.1) by $1 \equiv \rho/\rho$ and denoting the kernel

$$h_\theta(\rho, z) \equiv \frac{\mu}{4\pi|AB|} \frac{z(z\cos\theta + \rho\sin\theta)}{\rho^2\left(z^2 + \rho^2\right)^{3/2}} e^{-\mu|AB|\frac{z + \rho\tan(\theta/2)}{\sqrt{z^2 + \rho^2}}}, \tag{3.3}$$

we can reduce (3.1) to

$$\xi_\theta^{AB} = \int_0^{|AB|} dz \int_0^{2\pi} d\psi \int_0^{R_\theta(z)} h_\theta(\rho, z) f(\psi, \rho, z)\rho d\rho\,. \tag{3.4}$$

It follows from this representation that the inner double integral

$$\int_0^{2\pi} d\psi \int_0^{R_\theta(z)} h_\theta(\rho, z) f(\psi, \rho, z)\rho d\rho \tag{3.5}$$

in (3.4) is a value of the convolution of the function f section by the plane parallel to xOy with the coordinate z, and the radially symmetric kernel $h_\theta(\rho, z)$ with a circular support of radius $R_\theta(z)$. The outer integral $\int_0^{|AB|} dz$ represents the X-ray transform (along the lines parallel to the direction z) of the slice-by-slice blurred versions of the activity function f.

Figure 2 shows numerical results illustrating the structure of the 3D scatter kernel h_θ. In the experiments, $\mu = const = 0.096 cm^{-1}$, $\theta = 30°$ (corresponding to scattered photons with energy 450keV detected by a detector with perfect energy resolution) and $h = 30 cm$. Kernel values were computed in the centers of $0.5 \times 0.5 \times 0.5 cm^3$ voxels of image of size $60 \times 60 \times 60$ voxels. The kernel support has a spindle shape, and the kernel's larger values are concentrated around detector A, rapidly decreasing in direction to detector B. It also decreases rapidly in lateral direction, from the vicinity of the central line AB to the kernel's borders. We can see that the kernel gives larger weights to the activity for areas close to A and smaller weights to the kernel region around B (Figure 2 (a)). We conclude therefore, that with PET detectors tightly positioned around the patient, there emerges additional information from scatter about activity hot spots located close to the patient's body periphery. We have further repeated the calculations for a more realistic case, representing range of scattering angles given by 12% energy resolution detectors (FWHM of the Gaussian energy resolution function was 60 keV). Obtained kernel has a very similar shape to the ideal one. Nearly identical, longitudinal and lateral profiles of both kernels are shown in Figure 2 (b), (c).

The slice-by-slice convolution model (3.4) of the projection formation is known in Transmission Electron Microscopy [9] and it is proven to be invertible [13] provided full data are available. The reconstruction technique derived was named as the Defocus-gradient Corrected Backprojection (DGCBP) algorithm. The algorithm was tested thoroughly in [16]. Thus, we have reduced the simplified Compton scatter model to the already developed reconstruction technique.

4 Monte Carlo simulation algorithm

We performed Monte Carlo simulations using our software codes [1], [15], [30] with allowance for the physical effects in the PET modality. The main components of the MC algorithm used in this study are:

- Step 1. *Positron annihilation point sampling.*

  We sample point r of positron origination inside the activity domain. This point becomes the point of annihilation. We generate samples from the uniform distribution inside the sphere of activity.

- Step 2. *Sampling of the initial direction of a photon.*

  As a result of the positron-electron annihilation, two photons are emitted in opposite directions. Because of the isotropy of initial directions, the direction of the first photon $\omega = (\omega_1, \omega_2, \omega_3)$ is uniformly chosen on a unit sphere. Then we track the photon moving in the direction ω.

- Step 3. *Calculation of a free path in a medium.*

  Using an exponential decrease in the photon survival probability with increasing a distance, we can find a single photon free path in the medium. When leaving the object volume, the photon is checked for getting onto the detector. If the photon hits the detector, we record the detector's position and proceed with tracing the other photon in the direction $-\omega$. In the case the photon does not hit a detector, we stop tracing it and go to Step 1. In case the photon is still inside the object, we continue random sampling.

- Step 4. *The types of photon-medium interaction.*

  For determination of the photon-medium interaction type, we calculate probabilities of absorption, the Compton and Rayleigh scatters denoted by P_a, P_c, P_r respectively. If a random number $\alpha < P_a$, then a photon is attenuated and its trajectory is not further traced. If $\alpha > P_a$, then the photon undergoes scattering and the type of a scatter has to be detected. In case of $\alpha < P_r$, a photon scatter is of the Rayleigh type, otherwise it is of the Compton type.

- Step 5. *The Rayleigh scatter.*

  If a photon has undergone the Rayleigh scatter, then we choose a new direction ω', using the Rayleigh scattering function.

- Step 6. *The Compton scatter.*

  In case of the Compton scatter, not only the direction but also the energy of a photon changes. Probability that a scattered photon has energy on the interval from E to E' depending on a random number α is estimated from the equation

$$\int_{E}^{E'} \frac{d\tilde{\sigma}_C}{dE} dE = \alpha, \tag{4.1}$$

where $d\tilde{\sigma}_C/dE$ is the Compton scatter differential cross-section normalized to unity for the energies from E to $E + dE$. It is calculated using the Klein-Nishina formula [6]. Solving equation (4.1) is a cumbersome procedure. For its speed-up, we use a preliminarily calculated 2D look-up table with the solution to (2.15) with a certain precision on regular meshes in terms of E and α. The calculated value of the scattered photon energy provides us with the cosine of the scattering angle:

$$\nu = 1 + E_0/E - E_0/E', \tag{4.2}$$

where E_0 is the zero mass energy of the electron. Further sampling with equal probabilities within the range of 0 up to 2π of the azimuthal angle of the scatter, we can find a new direction of the photon after a scatter event.

- Step 7. *Return with Exit*.

  We return to Step 3 and trial again a free path and repeat this procedure till either the photon hits the detector or leaves the volume, or becomes absorbed.

5 Numerical Simulation

The numerical experiments were performed on a numerical cylindrical phantom (similar to that used in [22]) filled in with water of $8cm$ radius and large length. The geometry of the four source Configurations labeled as 1, 2, 3, 4 is shown in Figure 3. The sources are the spherical uniform emitters of 0.9cm radius and unit activity. Their centers C_1, C_2, C_3, C_4 are located in the plane yOz with the coordinates

$$C_1 = (0, 0, 8), \quad C_2 = (0, 0, 12), \quad C_3 = (0, -4, 8), \quad C_4 = (0, 0, 4)\,. \tag{5.1}$$

The detector lines $A = \{A_i\}$ and $B = \{B_i\}$ of length $16cm$ consist of 100 crystals each. The crystal centers have the coordinates

$$A_i = (0.0, 8.0 - (i - 0.5)\delta, 0.0), \quad B_i = (0.0, 8.0 - (i - 0.5)\delta, 16.0)\,. \tag{5.2}$$

Here, $\delta = 0.16$ cm is diameter of an element on the detector.

We simulated the following intensity

$$M_\theta \approx \left(\pi\delta^2/4\right)^2 \xi_\theta^{AB} \tag{5.3}$$

using Monte Carlo techniques. Cross-section data were taken from the Hubble-Seltzer tables [8]. There were totally 10^{11} histories generated (the computation time with Intel Core i3 CPU was 25 hours) in the course of the MC simulation calculations of a single projection. The pseudorandom number generator following the method described in [18] was implemented. The calculations of projections ξ_θ and M_θ were performed for Configurations 1 through 4 using formulas (4.2) and (5.3) for 100 pairs of the opposing crystalls (A_i, B_i).

The 1D sections of 2D projections of Configurations 1 through 4 for a single scatter with the parameter $\theta = 60°$ are shown in Figure 4. We scaled the projections ξ_θ and M_θ by searching for maxima, fixing at the global maximum point, and then bringing them to the interval [0, 10].

In the geometric modeling, the borders of the cylinder $D(\mu)$ and the 3D spindle kernel support V_θ were taken into account, so that integrations were performed over intersection of the domains $D(\mu)$ and V_θ. An example of the influence of a complex shape of borders of the intersection $D(\mu) \cap V_\theta$ is seen as a peculiar scatter projection profile of the sphere number 3 in Figure 4 (c). The example clearly shows that although the analytical formula of the forward scatter model is available, an adequate and consuming geometric modeling in practical situations is necessary.

6 Discussion

For a PET device consisting of limited size detectors, data are not collected for some of the lines of response. Because of the limited size of the detector, the second photon v would miss the detector B, moving to point Q (Figure 1 (b)), if the scatter did not happen. The scattered photon, denoted by v', travels from S to the detector point B. Thus a scatter event carries an extra information from direction defined by line AS which would be otherwise not available if we were collecting only true events. On the other hand, these scatter events contaminate true events on the line AB if they are not rejected. It is attractive to investigate non-conventional reconstruction approaches that make use of the information in the scattered photons. These photons are a potential source of the information about those paths through the domain for which two unscattered back-to-back photons cannot be intercepted by a detector pair. This additional information might be useful for the dual detector systems with incomplete data [19].

With improvements in the detector energy resolution, the Compton scatter energy-selected imaging could be a source of new opportunities [10], [11]. Validated scatter models of the same generality as mathematical models known as X-ray and the Radon transforms might be a potential starting point for developing the new scatter correction algorithms and multispectral methods aimed at extracting information from the scatter projections formed with different energies. The closely related integral transforms (2.14) and (2.15) describing a single scatter (with a certain scattering angle) projection formation were derived from the total scatter formula (1.3). We hypothesize that this idealized model can be used in answering a question: whether the emitter activity f can be reconstructed from the data ξ_θ^{AB} and what in principle is a mathematical reconstructive potential of such data.

7 Conclusions

This work is a part of investigation of generalized Radon transforms and non-conventional reconstruction approaches that make use of the information in the scattered photons. In this paper, we have compared the proposed idealized analytical formula for the single scatter estimation with independent Monte Carlo simulation. A good match of statistically simulated scatter projections of a digital phantom and those calculated with the integral transform shows that with our idealized assumptions, we did not ignore influential factors of original physical phenomena. We conclude that the forward transform simulating the Compton scatter can serve as a mathematical basis for developing the algorithms for its inversion.

Acknowledgments.

The authors thank Per Christian Hansen, Joel Karp and Lucretiu Popescu for the fruitful discussions.

The content is solely the responsibility of the authors and does not necessarily represent the official views of the National Institutes of Health. This work was supported in part by the NIH grants R01-EB023274 and R01-CA113941. The first author was supported in part by the Siberian Branch of the Russian Academy of Sciences (project no. 0315-2016-0003).

Bibliography

[1]. Anikonov DS, Kovtanyuk AE, Prokhorov IV, Transport Equation and Tomography, Inverse and Ill-Posed Problems Series, 30, VSP, Boston-Utrecht, 2002.

[2]. Berg E and Cherry SR, Innovations in instrumentation for positron emission tomography Semin. Nucl. Med 48 (2018), 311–331.

[3]. Berker Y and Li Y, Attenuation correction in emission tomography - A review Med. Phys 43 (2016), 807–832. [PubMed: 26843243]

[4]. Buvat I, Castiglioni I, Feuardent J and Gilardi MC, Unified description and validation of Monte Carlo simulators in PET Phys. Med. Biol 50 (2005), 329–346. [PubMed: 15742948]

[5]. Conti M, Hong I and Michel C, Reconstruction of scattered and unscattered PET coincidences using TOF and energy information Phys. Med. Biol 57 (2012), 307–317.

[6]. Fano U, Spencer LV and Berger MJ, Penetration and diffusion of X-rays, Encyclopedia of Physics 38/2, Springer-Verlag, Berlin, 1959.

[7]. Gillam JE and Rafecas M, Monte-Carlo simulations and image reconstruction for novel imaging scenarios in emission tomography, Nucl. Instrum. Meth. A 809 (2016), 76–88.

[8]. Hubbell JH and Seltzer SM, Tables of X-Ray Mass Attenuation Coefficients and Mass Energy-Absorption Coefficients 1 Kev to 20 Mev for Elements Z = 1 to 92 and 48 Additional Substances of Dosimetric Interest, NISTIR 5632 (1995).

[9]. Jensen GJ and Kornberg RD, Defocus-gradient corrected back-projection, Ultramicroscopy 84 (2000), 57–64. [PubMed: 10896140]

[10]. Jones T and Townsend D, History and future technical innovation in positron emission tomography, J. Med. Imaging 4 (2017), 011013.

[11]. Jones KC, Redler G, Templeton A, Bernard D, Turian JV and Chu JCH, Characterization of Compton-scatter imaging with an analytical simulation method, Phys. Med. Biol 63 (2018), 025016. [PubMed: 29243663]

[12]. Kazantsev IG, Matej S and Lewitt RM, Geometric model of single scatter in PET, in: IEEE Nuclear Science Symposium Conference Record 5 (2006), 2740–2743.

[13]. Kazantsev IG, Klukowska J, Herman GT and Cernetic L, Fully three-dimensional defocus-gradient corrected backprojection in cryoelectron microscopy, Ultramicroscopy 110 (2010), 1128–1142. [PubMed: 20462697]

[14]. Kazantsev IG, Olsen UL, Poulsen HF and Hansen PC, A spectral geometric model for Compton single scatter in PET based on the single scatter simulation approximation, Inverse Problems 34 (2018), 024002.

[15]. Kim A and Prokhorov IV, Monte Carlo method for non-stationary radiative transfer equation in inhomogeneous media, in: Proc. SPIE, Tomsk, Russia (2016), 100350Z.

[16]. Klukowska J and Herman GT, Reconstruction from Microscopic Projections with Defocus-Gradient and Attenuation Effects, in: Computational Methods for Three-Dimensional Microscopy Reconstruction, Birkhauser, Basel (2014), 157–186.

[17]. Kondic M and Jupiter C, Noninvasive method for determining the three-dimensional density distribution in an inspected object employing modulation of compton-scattered gamma signals, in: Proc. IEEE Nucl. Sci. Symp. Med. Imag. Conf., Knoxville, TN, USA (2010), 70–79.

[18]. L'Ecuyer P and Cote S, Implementing a Random Number Package with Splitting Facilities, ACM Trans. on Math. Software 17 (1991), 98–111.

[19]. Narayanan D and Berg WA, Dedicated Breast Gamma Camera Imaging and Breast PET: Current Status and Future Directions, PET Clinics 13 (2018), 363–381. [PubMed: 30100076]

[20]. Natterer F and Wübbeling F, Mathematical Methods in Image Reconstruction, SIAM Philadelphia, 2001.

[21]. Norton SJ, Compton scattering tomography, J. Appl. Phys 76 (1994), 2007–2015.

[22]. Riauka T and Gortel W, Photon propagation and detection in single-photon emission computed tomography — an analytical approach, Med. Phys 21 (1994), 1311–1321. [PubMed: 7799876]

[23]. Rigaud G and Hahn BN, 3D Compton scattering imaging and contour reconstruction for a class of Radon transforms, Inverse Problems 34 (2018), 075004.

[24]. Rigaud G, Nguyen MK and Louis AK, Modeling and simulation results on a new Compton scattering tomography modality, Simul. Model. Pract. Th 33 (2013), 28–44.

[25]. Sun H and Pistorius S, A Geometric Model to Characterize Annihilation Positions Associated With Scattered Coincidences in PET: A Simulation-Based Study, IEEE T. Comput. Imag 2 (2016), 101–108.

[26]. Truong TT and Nguyen MK, Recent developments on Compton scatter tomography: theory and numerical simulations, in: Numerical SimulationâĂŤFrom Theory to Industry, INTECH Publications, Editors: Andriychuk M (2012), Chapter 6.

[27]. Watson CC, New, faster, image-based scatter correction for 3D PET, IEEE Trans. Nucl. Sci 47 (2000), 1587–94.

[28]. Webber JW and Lionheart WRB, Three dimensional Compton scattering tomography, Inverse Problems 34 (2018), 084001.

[29]. Webber JW and Holman S, Microlocal analysis of a spindle transform, Inverse Probl. Imaging 13 (2019), 231–261.

[30]. Yarovenko IP, Numerical experiments with the inhomogeneity indicator in positron emission tomography, J. of Applied and Industrial Mathematics 2 (2012), 261âĂŞ–268.

[31]. Zaidi H, Scatter modelling and correction strategies in fully 3-D PET, Nucl. Med. Commun 22 (2001), 1181–1184. [PubMed: 11606882]

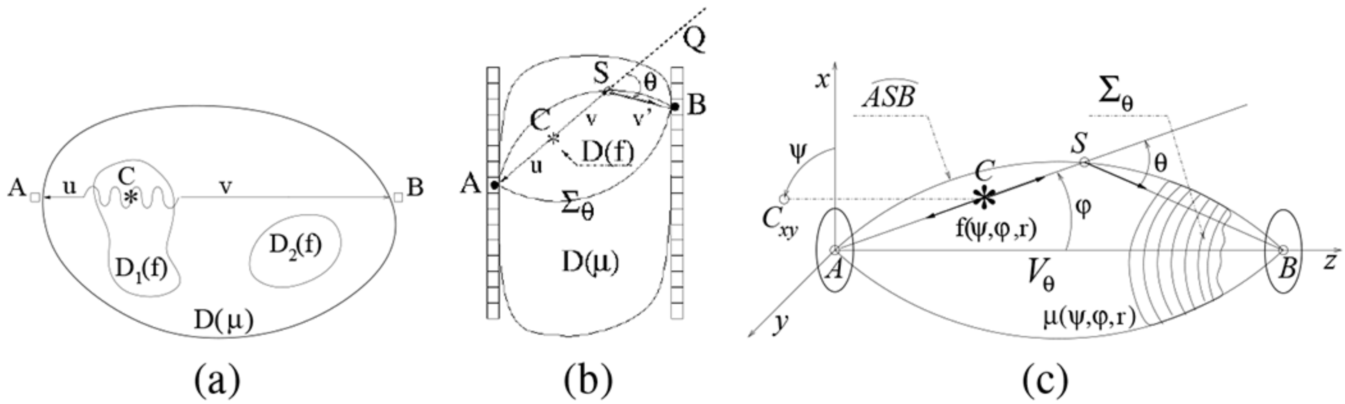

Figure 1.

Geometry of data formation in PET. (a) Primary photons (u, v) of energy E = 511 keV, originating from annihilation point $C \in D(f) = D(f_1) \cup D(f_2)$. The domain $D(\mu)$ is the support of the attenuation map μ and $D(f)$ is the support of the activity function f. (b) Single Compton scatter happens in point $S \in D(\mu)$, v' is a photon v with energy E', scattering with angle θ. The Q is a hypothetical point which is out of dual PET detector limits. Detector A records unscattered photons u; B records photons v'. (c) S is a scattering point with the polar coordinates (ψ, φ, $|AS|$). Σ_θ is the isogonic surface of the spindle-shaped 3D rotation body V_θ generated by the circle arc ASB, $\measuredangle ABS = \theta - \varphi$.

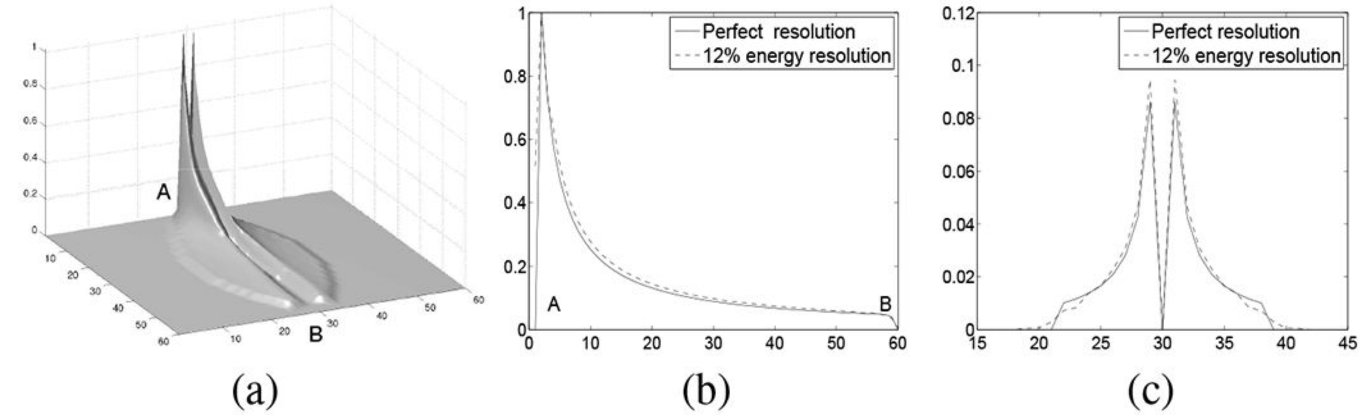

Figure 2.
The 3D scattering kernel h_θ, $\theta = 30°$; (a) 3D view of 2D sectional image of h_θ. (b) Longitudinal profiles of kernels with excellent and 12% resolution from A to B at 30-th column; (c) Lateral profile of same kernels at the 30-th row.

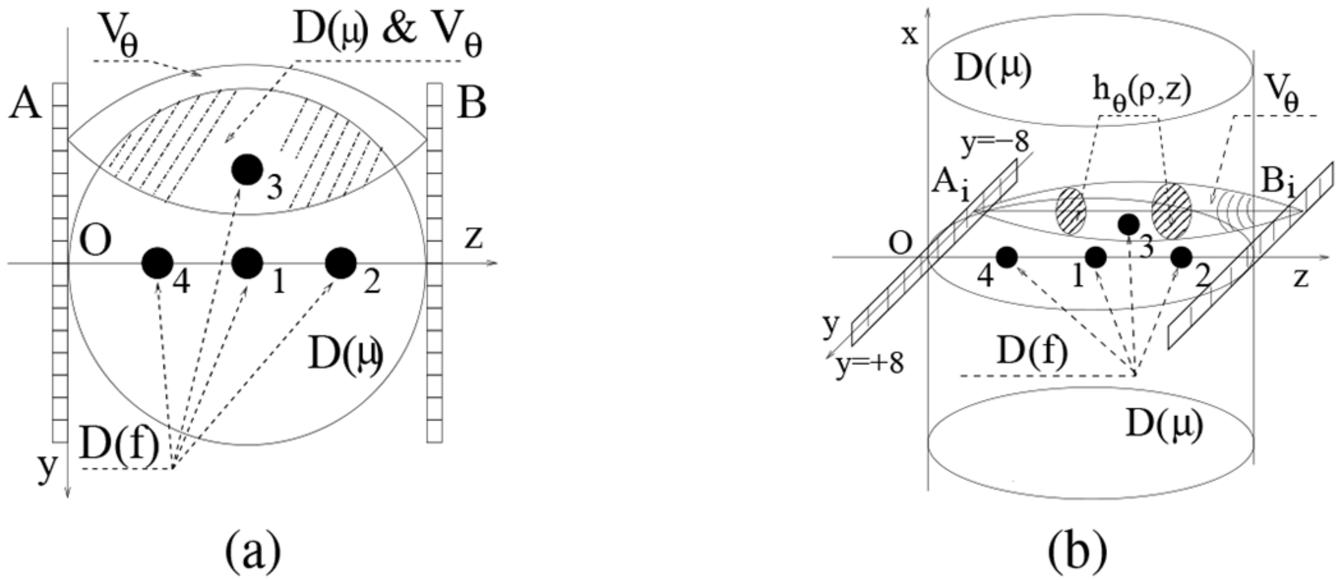

Figure 3.

Geometry of the source Configurations 1, 2, 3, 4. (a) The 2D view of section *yOz*, $D(\mu)\& V_\beta \equiv D(\mu) \cap V_\theta$. (b) The general 3D view.

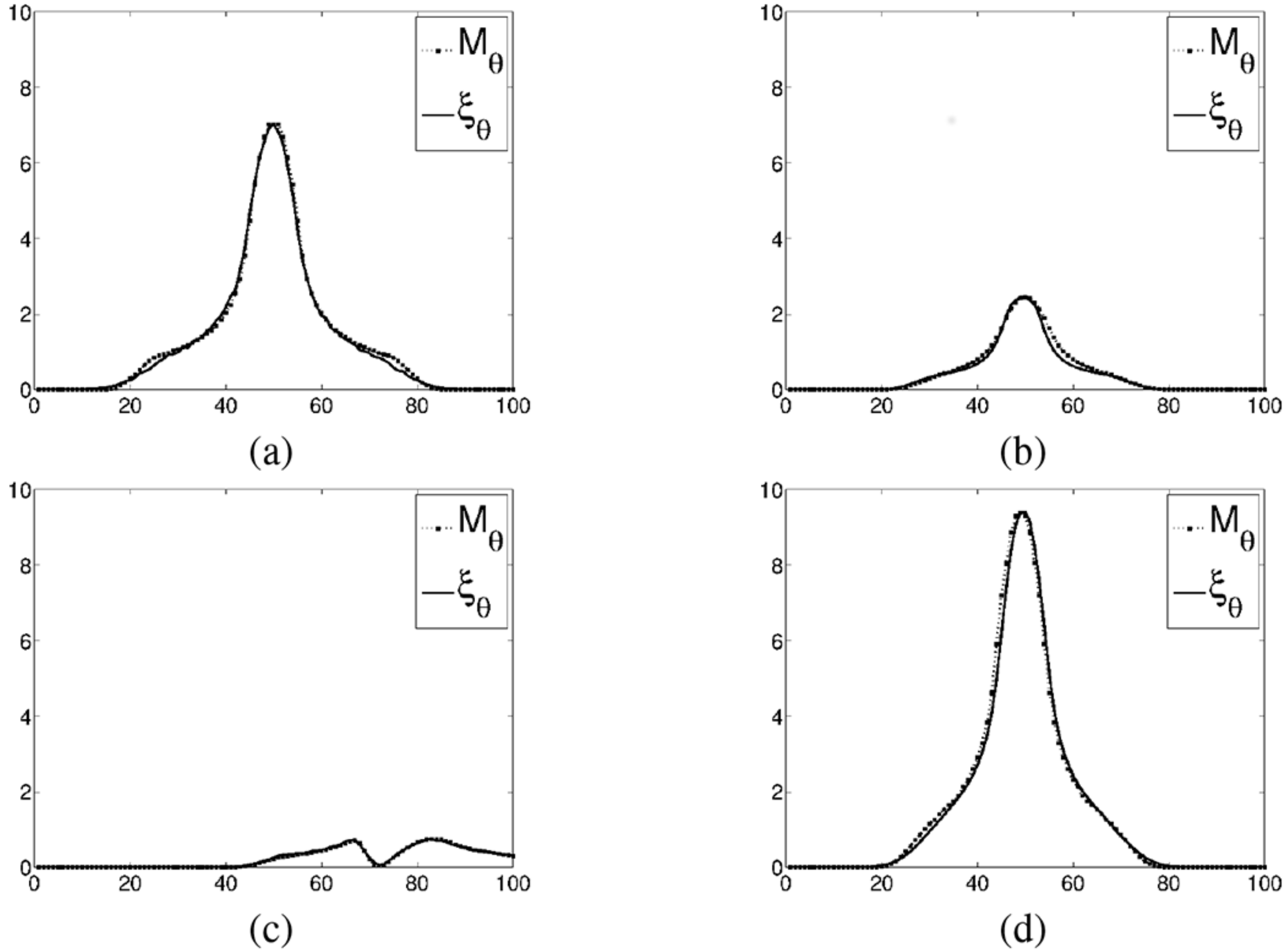

Figure 4.

Profiles of scatter projections M_θ and ξ_θ generated with Monte Carlo simulation (dotted) and formula (2.15) (solid). Profiles (a), (b), (c) and (d) represent the scatter contributions of $\theta = 60°$ single scatter photons for Configurations 1, 2, 3 and 4 (Figure 3), respectively.